1/*f* noise in a thin stochastic layer described by the discrete nonlinear Schrödinger equation

C. L. Pando L.[1] and E. J. Doedel[2]
[1]*IFUAP, Universidad Autónoma de Puebla, Apartado Postal J-48, Puebla, Puebla 72570, Mexico*
[2]*Concordia University, 1455 Boulevard de Maisonneuve West, Montreal, Quebec, Canada H3G 1M8*
(Received 20 March 2006; revised manuscript received 25 September 2006; published 23 January 2007; corrected 26 January 2007)

We investigate the nonlinear dynamics in a trimer, described by the one-dimensional discrete nonlinear Schrödinger equation, with periodic boundary conditions in the presence of a single on-site defect. We make use of numerical continuation to study different families of stationary and periodic solutions in this Hamiltonian system. Taking into account a suitable Poincaré section, we are able to study the dynamics of a generic thin stochastic layer in this conservative system. Our results strongly suggest that intermittency, on the one hand, and transport between two almost invariant sets, on the other hand, are relevant features of the chaotic dynamics. This behavior arises as a result of the formation of the above mentioned stochastic layer connecting two hyperbolic fixed points of the Poincaré return map. We find that the transit times, the time intervals to traverse some suitable sets in phase space, generate $1/f$ noise. Its origin is explained in terms of a hopping mechanism in a suitable discrete state space of transit times. A qualitatively similar behavior is also found in the standard map, which shows the generic nature of this mechanism. As a physical application of our results, we consider a possible experiment in a ring of weakly coupled Bose-Einstein condensates (BECs) with attractive interactions, where intermittent bursts of the relative phase of two spatially symmetric BECs take place.

DOI: 10.1103/PhysRevE.75.016213 PACS number(s): 05.45.−a, 42.65.Tg, 87.10.+e, 42.25.Bs

I. INTRODUCTION

Typical Hamiltonian systems with two degrees of freedom have a divided phase space consisting of regular and chaotic regions, where the former regions are organized in a hierarchical way [1]. One important property of chaotic trajectories is the trapping that these undergo in the neighborhood of hierarchical structures of Kolmogorov-Arnold-Maser (KAM) islands and cantori [2,3]. The stickiness to these invariant structures brings about intermittency, which is characterized by long-range correlations [2,4]. In the present paper, we will explore the long-range correlations in a complex thin stochastic layer (TSL) described by the discrete nonlinear Schrödinger equation (DNLSE). In Hamiltonian systems with two degrees of freedom, thin stochastic layers arise near unperturbed separatrices destroyed by suitable small perturbations [1]. Stochastic layers have been studied within the context of several physical systems [5], where the exponentially small width is one of their main features [1].

An important Hamiltonian model that describes a lattice of coupled anharmonic oscillators is the DNLSE [6]. Indeed, the DNLSE has been derived from the discrete Klein-Gordon equation in the limits of small-amplitude oscillations and weak intersite couplings [7]. The DNLSE describes a large class of discrete nonlinear systems such as optical fibers [8,9], polarons [10], small molecules such as benzene [10], and, more recently, dilute Bose-Einstein condensates (BECs) trapped in a multiwell periodic potential [11]. We will consider the nonlinear dynamics of the DNLSE describing a ring consisting of three sites, the trimer, in the presence of a single defect. This defect characterizes the natural frequency mismatch among oscillators [6]. In a BEC, this kind of defect can be created with additional lasers or magnetic fields [11].

The DNLSE is a vast subject with many different and relevant issues such as the dynamics of discrete breathers in one- or two-dimensional infinite lattices [6]. We will concentrate on the special issue concerning the onset of instabilities and chaos in the DNLSE in lattices with a small number of sites. The DNLSE is a nonlinear Hamiltonian system with M degrees of freedom, where M refers to the number of oscillators. The DNLSE, as is well known, has two constants of motion [6]. Therefore, when $M=2$, the DNLSE is integrable. However, when $M\geq 3$, the DNLSE can exhibit an amazing degree of complexity. The chaotic dynamics for $M=3$ and 4 was studied, to our knowledge, for the first time almost two decades ago [12]. These authors underlined the fact that the DNLSE is generic in the spirit of modern nonlinear science, putting forward several molecular models described by the DNLSE. The nonlinear dynamics for a small number of oscillators has been considered since then [13]. Most of these studies, however, did not take into account the presence of a defect, which is central to our study. For $M=3$, symmetry arguments show that the dynamics is that of an area-preserving two-dimensional map. As a result, it provides a rich behavior, which is of interest to the aforementioned physical systems and, in particular, for both theory and experiment of BECs. When $M=3$, the passage of a trajectory from one stochastic region in phase space to another is blocked by KAM surfaces [1]. This is no longer true when $M>3$, where Arnold diffusion can take place. Therefore, generically the motion will spread out over an entire system of intersecting stochastic layers [1]. Indeed, in the context of the DNLSE, Arnold diffusion was considered for $M=4$[14].

In recent work [15,16], we have studied the nonlinear dynamics of the DNLSE with $M=7$ in the presence of a single one-site defect. In [15,16], we found several families of stationary solutions, whose unstable orbits trigger interesting complex dynamics. Moreover, relevant information on the chaotic behavior was found by considering suitable Poincaré cycles [16]. These Poincaré cycles give a better

understanding of the robust properties in this system. On the one hand, these cycles enabled us to study the self-trapping chaotic regime, where some peculiar behavior, typical of Arnold diffusion, arises. On the other hand, in continuous time, the difference of actions in certain pairs of oscillators switch sign almost simultaneously [15–17]. In this regime, the statistics of the Poincaré cycles suggest, surprisingly, an almost Markovian behavior in spite of the fact that the oscillators are to a good extent phase locked.

In this work, we study the DNLSE with periodic boundary conditions in the presence of a single on-site defect when $M=3$. In this study, we made use of numerical continuation, which allowed us to find families of stationary and periodic solutions along with their linear stability properties. Next, we consider a generic chaotic solution which behaves as a complex thin stochastic layer over a wide range of parameters. We use a suitable Poincaré section, which, being related to the geometry of the solution, suggests the set of variables to consider. This complex thin stochastic layer displays, on the one hand, intermittency and, on the other hand, transport between two almost invariant regions. As a result, our TSL solution shows a robust $1/f$ noise. The $1/f$ noise phenomenon has attracted the attention of physicists over several decades as a result of the underlying long-range correlations, which have been found to be ubiquitous in systems ranging from DNA and physiology to econophysics [18]. In Hamiltonian systems, a generic mechanism that gives rise to $1/f$ noise was associated with the presence of a self-similar hierarchy of cantori [4]. More recently, it was shown that $1/f$ noise is present in the spectral fluctuations in chaotic quantum systems [19].

This paper consists of eight sections. In Sec. II, we consider the DNLSE and illustrate it in the context of BECs. In Sec. III, we study the linear stability of different families of stationary and periodic solutions using numerical continuation. In Sec. IV, we consider a suitable Poincaré section to study the dynamics of a robust thin stochastic layer. In Sec. V, we discuss intermittency and transport in the stochastic layer. In Sec. VI, we investigate the characteristic $1/f$ noise in the transit times, to cross some suitable neighborhoods in phase space, in both the trimer and the standard map. In Sec. VII, we study the evolution of measurable physical quantities in our BEC system to consider a possible experiment. Finally, in Sec. VIII we give our conclusions.

II. THE MODEL

We study a ring of three coupled nonlinear oscillators with periodic boundary conditions in the presence of a single on-site defect, whose equation of motion is given by Eq. (2). To illustrate the physical background of our model within the context of a BEC, we consider an array of weakly coupled condensates, whose equation of motion is given by

$$i\frac{\partial \Psi_m}{\partial t} + \Delta_m \Psi_m + K(\Psi_{m-1} + \Psi_{m+1}) + \rho|\Psi_m|^2\Psi_m = 0, \quad (1)$$

where Ψ_m stands for the condensate complex amplitude in the mth well, ρ is the nonlinear coefficient arising from the interatomic interaction, K is proportional to the microscopic tunneling rate between adjacent sites, Δ_m stands for the on-site defect and is proportional to an external field superimposed on the lattice, and, finally, t is the time [11]. By introducing the dimensionless amplitude $\psi_m=\sqrt{\rho/2K}\Psi_m \times\exp[-i(\Delta+2K)t]$, Eq. (1) transforms into the discrete nonlinear Schrödinger equation given by

$$i\frac{\partial \psi_m}{\partial \tau} + \delta_m\psi_m + (\psi_{m-1} + \psi_{m+1} - 2\psi_m) + 2|\psi_m|^2\psi_m = 0, \quad (2)$$

where $\delta_m=(\Delta_m-\Delta)/K$ stands for the defects, $\tau=Kt$, and Δ is any arbitrary number. As a result, the only explicit parameters of the DNLSE in Eq. (2) correspond to the defects δ_m. The positive sign before the nonlinear term indicates that we are considering an attractive interatomic interaction between the condensates, such as in the case of lithium atoms [20].

There are two integrals of motion in Eq. (2). The first is the Hamiltonian, from which Eq. (2) is derived [6]. It is given by

$$H = \sum_{m=1}^{M} (|\psi_m - \psi_{m+1}|^2 - |\psi_m|^4 - \delta_m|\psi_m|^2). \quad (3)$$

The second constant is the norm, which is given by

$$N = \sum_{m=1}^{M} |\psi_m|^2. \quad (4)$$

Here M stands for the number of condensates.

We can rewrite the DNLSE by transforming into action-angle variables (N_m, θ_m), where $\psi_m=\sqrt{N_m}\exp(-i\theta_m)$, to stress the physical meaning of the equations of motion. The equations for $N_m \geq 0$ and θ_m are the following:

$$\frac{dN_m}{d\tau} = 2\sqrt{N_m N_{m-1}}\sin(\theta_{m-1} - \theta_m) + 2\sqrt{N_m N_{m+1}}\sin(\theta_{m+1} - \theta_m),$$

$$\frac{d\theta_m}{d\tau} = 2 - \delta_m - \sqrt{\frac{N_{m-1}}{N_m}}\cos(\theta_{m-1} - \theta_m) - \sqrt{\frac{N_{m+1}}{N_m}} \times\cos(\theta_{m+1} - \theta_m) - 2N_m. \quad (5)$$

N_m stands for the atomic population of site m.

To find the DNLSE stationary solutions, we use the nonlinear map approach [21,22]. This map is obtained by setting $dN_n/d\tau=0$, and $\theta_n=\theta_m$, for any $n\neq m$ in Eq. (5). Moreover, we can define the frequency of the resulting periodic orbit by setting $d\theta_m/d\tau=\lambda$, where λ is a constant. Therefore, the stationary solutions have the form $\psi_m(\tau)=\sqrt{N_m}\exp(-i\lambda\tau)$. As a result, the following cubic map (CM) is obtained:

$$X_{n+1} = Y_n,$$

$$Y_{n+1} = (\Gamma_n - 2Y_n^2)Y_n - X_n, \quad (6)$$

where $\Gamma_n=2-\lambda-\delta_n$ and $Y_n=\sqrt{N_n}$. In the CM we will set $\Gamma_n=\Gamma=2-\lambda$ for which $\delta_n=0$. The Jacobian J of this map is area preserving, i.e., $J=1$. The fixed points $(\pm\sqrt{\Gamma/2-1}, \pm\sqrt{\Gamma/2-1})$ of the CM are elliptic for $2<\Gamma<4$. In this paper, the use of this fixed point, to construct an initial condition for the DNLSE, gives us the freedom to select the

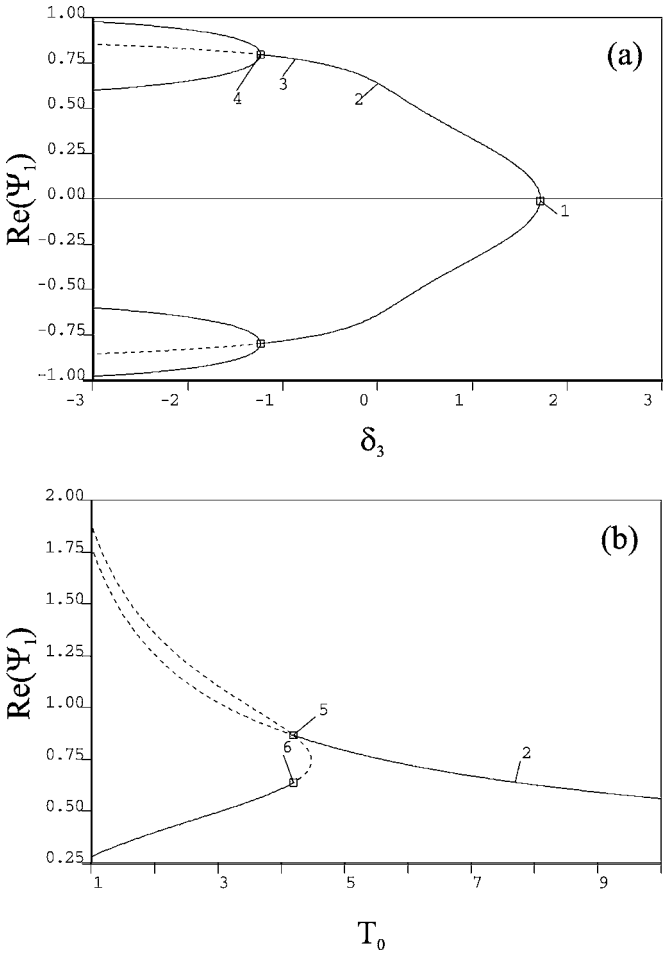

FIG. 1. (a) Plot of $\mathrm{Re}(\psi_1)$ versus δ_3 for families of stationary solutions. Here $\lambda=-2\pi/7.695\,29$. (b) Plot of $\mathrm{Re}(\psi_1)$ versus $T_0=-2\pi/\lambda$ for families of stationary solutions, where $\delta_3=0$. The solid and dashed lines stand for stable and unstable solutions, respectively.

number of oscillators within the ring. The search for the stability of these solutions is given in the next section.

In our previous publications [15–17,23], the number of oscillators in the ring was $M=6,7$. Using the above mentioned map, we found new families of stationary solutions by considering stable periodic orbits that surround a suitable elliptic point of the map. In [15–17,23], the number of oscillators in the ring is exactly determined by the periodicity of the orbit. Numerical continuation was further applied to find a complex dependence of the solutions on the defect parameter [15,16].

III. A FAMILY OF STATIONARY AND PERIODIC SOLUTIONS AND THEIR LINEAR STABILITY

The bifurcation diagram in Fig. 1(a), computed using the numerical bifurcation software AUTO [24,25], shows the real part of ψ_1, $\mathrm{Re}(\psi_1)$, versus δ_3 for stationary solution families of the DNLSE with three oscillators. The trivial solution $\psi_i=0$, where $i=1,2,3$, is stable, here meaning that the eigenvalues of the Jacobian evaluated at the stationary solutions all have zero real part. At the branch point, which is the bifurcation point with label 1, along the trivial family there are two eigenvalues equal to zero, giving rise to a secondary family of nontrivial solutions.

Along the secondary family we have $\psi_1=\psi_2\neq\psi_3$, except at the solution with label 1, where $\psi_1=\psi_2=\psi_3=0$, and at the solution with label 2, where $\delta_3=0$ and $\psi_1=\psi_2=\psi_3\neq 0$. Also, along the secondary family there are always two eigenvalues equal to zero, in view of the rotational invariance of the solutions of this family. At the secondary branch point, which is the solution with label 4, there are four zero eigenvalues, and the family becomes unstable to the left of this point, where its solutions have two real eigenvalues of the form r and $-r$, where r is real and depends on δ_3. Stationary solutions along the tertiary family that emanates from the secondary branch point, that is from the solution with label 4, have the property that ψ_1, ψ_2, and ψ_3 have different values, except at the solution with label 4, where $\psi_1=\psi_2$. Again, along the tertiary family there are always two eigenvalues equal to zero.

The bifurcation diagram in Fig. 1(b) shows $\mathrm{Re}(\psi_1)$ versus $T_0=-2\pi/\lambda$. The stationary solution with label 2 in Fig. 1(b) corresponds to the same solution with label 2 in Fig. 1(a), i.e., the solution with $\delta_3=0$ and $\psi_1=\psi_2=\psi_3\neq 0$. Stationary solutions, along the family that passes through the solution with label 2 in Fig. 1(b), have the property that $\psi_1=\psi_2=\psi_3\neq 0$, and their Jacobians have a double zero eigenvalue. To the right of the solution with label 5 all eigenvalues lie on the imaginary axis. At the solution with label 5 all eigenvalues are zero, while to the left of the solution with label 5 there are four real eigenvalues of the form r and $-r$, each being a double eigenvalue. Thus solutions of this family are unstable to the left of the solution with label 5. The latter is a branch point from which several families of stationary solutions arise. One of these families is represented in Fig. 1(b), namely, the family that carries the solution with label 5. Solutions along this family have the property that $\psi_1=\psi_2\neq\psi_3$, except at the solution with label 5. Note that the family contains another branch point, that also carries the solution with label 6, and that part of the family consists of stable stationary solutions. As mentioned, the solution with label 5 is multiple bifurcation point. In addition to the bifurcating solution family described above, for which $\psi_1=\psi_2\neq\psi_3$, there are two additional families that emanate from the solution with label 5, namely, families whose solutions satisfy $\psi_1=\psi_3\neq\psi_2$, and $\psi_2=\psi_3\neq\psi_1$, respectively. Thus the three families that emanate from the solution with label 5 are related through a permutation symmetry. In view of the Lyapunov center theorem [26], there are several families of periodic solutions that emanate from each stationary point. These results are shown in Table I, where the counts may not be valid at a discrete set of points.

As an example, consider the two families that emanate from the stationary solution at $\delta_3=-0.863\,333$, the solution with label 3, along the secondary family of stationary solutions. At this point the stationary solution has two zero eigenvalues and two pairs of purely imaginary eigenvalues with imaginary parts $\pm 3.207\,45$ and $\pm 0.778\,746$, giving rise to two families of periodic solutions, which we label as family 1 and family 2, respectively. Figure 2(a) shows the imagi-

TABLE I. Families of periodic solutions.

Stationary family	Periodic families
Trivial	3
Secondary (to the right of label 4)	2
Secondary (to the left of label 4)	1
Tertiary	2

nary part of ψ_1, $\mathrm{Im}(\psi_1)$, versus $\mathrm{Re}(\psi_1)$ for a selection of periodic solutions of family 1. Figure 2(b) shows $\mathrm{Re}(\psi_1)$ versus (scaled) time for a selection of periodic solutions of family 2. Small-amplitude oscillations are stable along both families, but both families contain also unstable solutions.

IV. THE POINCARÉ SECTION

Consider the stable stationary uniform solution for which $\delta_3=0$ and $\psi_i=\sqrt{1/3}$ for $i=1,2,3$, where $\lambda=-2/3$ and $T_0=3\pi$. The stability of this uniform solution is shown in Fig. 1(b). We added small random perturbations of the order of

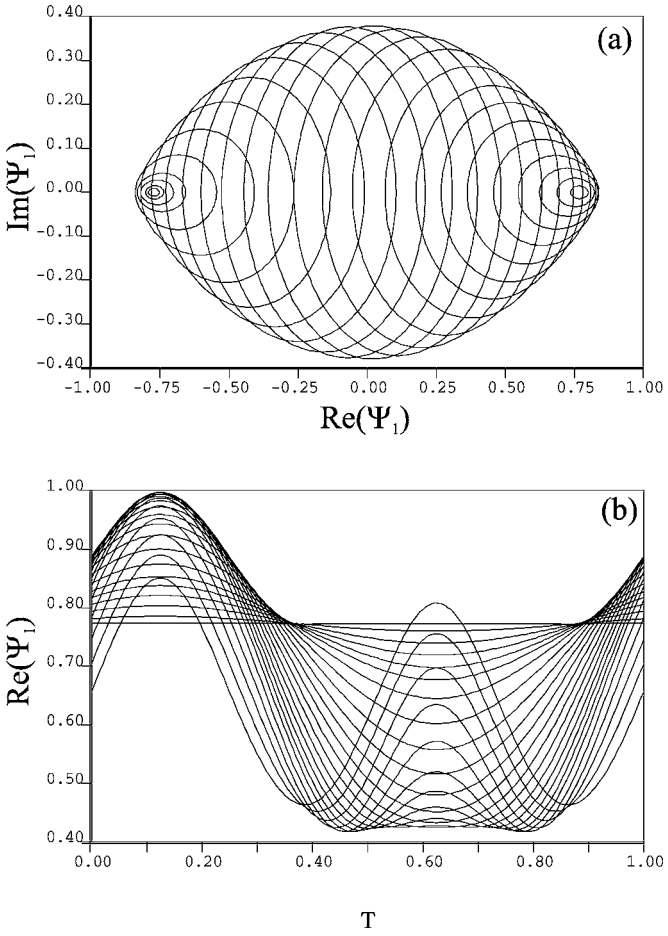

FIG. 2. (a) Plot of $\mathrm{Re}(\psi_1)$ versus $\mathrm{Im}(\psi_1)$ for a selection of periodic solutions of family 1. (b) Plot of $\mathrm{Re}(\psi_1)$ versus dimensionless time T in units of the normalized period for a selection of periodic solutions of family 2. Both family 1 and family 2 contain stable and unstable orbits.

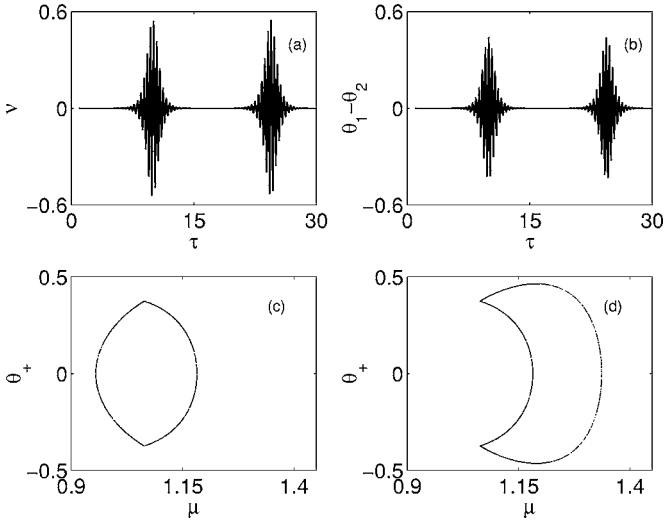

FIG. 3. (a) Continuous-time plot of $\nu=N_1-N_2$ versus τ for the TSL, where $\delta_3=-16/15$. (b) $\theta_1-\theta_2$ versus τ for the same trajectory shown in (a). (c) Projection of the Poincaré return map onto the plane (μ,θ_+) for a long time interval. This is the projection of the region with label A. (d) Same as (c), but for a consecutive long time interval. This is the projection of the region with label B. Both projections belong to the same TSL. In (a) and (b) τ in Eq. (2) has been rescaled by dividing by 3π.

10^{-7} to this stationary solution to obtain a set of initial conditions. Typically, as the parameter $\delta_3<0$ increases in absolute value, we find a transition from quasiperiodic to chaotic solutions for the set of initial conditions. The qualitative picture that emerges is, therefore, that of an initial condition moving away from the centers, which are given in Fig. 1(a), as δ_3 changes. As in typical Hamiltonian systems, this leads to a closer vicinity to stochastic layers where chaotic behavior occurs. Stochastic layers are separated from each other by KAM curves and motion from one layer to another is forbidden [1]. Notice that an increase in the absolute value of $\delta_3<0$ leads to an increase in the energy, while the norm of our solutions remains constant.

In order to consider a suitable Poincaré section of our solution, we define the new variable $\nu\equiv N_1-N_2$. Our chaotic solution intersects the Poincaré section transversally when $\nu=0$ and $d\nu/d\tau>0$. In Fig. 3(a), where $\delta_3=-16/15$, we observe that in continuous time the bursting behavior of ν is followed by laminar intervals. During these laminar intervals, we find that $\nu\approx 0$ and, in addition, ν becomes exactly zero several times. Moreover, the laminar and bursting intervals of the phase difference $\theta_1-\theta_2$ coincide to a good extent with those of ν, as suggested by Fig. 3(b). In addition, the dynamically relevant phases of the two symmetric oscillators show phase synchronization, namely, $|\theta_{1,2}-\theta_3|<0.8$. These features are typical in continuous time.

The DNLSE is an autonomous Hamiltonian flow with the aforesaid pair of constants of motion and two dynamically relevant phases. As a result, this system has four vanishing Lyapunov exponents and the associated map is two dimensional. The two-dimensional surface, where the Poincaré return map is located, is given by the following manifold:

$$H - N\Bigg(2 - \sin^2(\mu)\cos(2\theta_-) - \frac{|\sin(2\mu)|}{\sqrt{2}}[\cos(\theta_+ + \theta_-) + \cos(\theta_+ - \theta_-)] - \frac{N}{2}\sin^4(\mu) - N\cos^4(\mu) - \delta_3\cos^2(\mu)\Bigg) = 0, \quad (7)$$

where $\mu = \arccos(\sqrt{N_3/N})$, $\theta_+ = \frac{1}{2}(\theta_1 + \theta_2 - 2\theta_3)$, $\theta_- = \frac{1}{2}(\theta_1 - \theta_2)$. We will use these variables in what follows. This two-dimensional surface has been obtained by considering the equations for H, N, and $\nu = 0$. We have numerically tested its validity.

V. DEFECT INDUCED INTERMITTENCY AND TRANSPORT

A. The mechanisms

We now focus on the dynamics at the Poincaré section. For values of δ_3 roughly between $-13/15$ and $-19/15$ and using the set of initial conditions of the last section, the dynamics of the Poincaré return map displays typically intermittency as well as transport between two distinct regions of phase space. In Figs. 3(c) and 3(d) we consider the projection of the return map onto the plane (μ, θ_+). Figures 3(c) and 3(d), which we relate to region A and region B, respectively, show the evolution of this map during two consecutive long time intervals when $\delta_3 = -16/15$. Each time interval is composed typically of roughly 10^5 mapping iterations. The return map suggests that there is a mechanism for transport between the two regions. In an almost invariant region [27], such as regions A and B, typical points are mapped into the region itself with high probability. Therefore, one has to deal with transition probabilities for these two different sets. In spite of the fact that we have about 10^6 mapping iterations, the transitions between these two regions occur just a few times. The concept of the separatrix is useful to understand the transport mechanism between regions A and B. Thus, we first point out that the separatrix partitions phase space into disjoint regions [28]. Technically, the separatrix is formed by taking the union of segments of the stable and unstable manifolds of suitable fixed points of the Poincaré return map [28]. A trajectory crosses the separatrix through the turnstile, which is the region of phase space mediating transport across the separatrix [28]. Specifically, our simulations suggest that there is a separatrix which defines the transition from region A to region B, and vice versa. As for the corresponding fixed points of the return map, there are two symmetric hyperbolic fixed points, whose manifolds presumably bring about the aforementioned separatrix.

An important feature of the TSL is the intermittency that the orbit displays when crossing two symmetric trapping regions (STRs). The intermittency is appreciated in Fig. 4(d), where we have chosen just a few hundred consecutive iterations of μ at the Poincaré section. The two STRs are small neighborhoods which contain the intersections of the approximately smooth curves of Figs. 4(a)–4(c), where the two aforementioned hyperbolic fixed points are located. In Figs. 4(a)–4(c), we consider the projection of the return map onto the planes (θ_-, θ_+), (μ, θ_+), and (μ, θ_-), respectively, for $\delta_3 = -16/15$. The coordinates of these hyperbolic fixed points are $(\mu, \theta_+, \theta_-) \approx (1.064, 0.37, 0.000\,15)$ and $(\mu, \theta_+, \theta_-) \approx (1.064, -0.37, 0.000\,15)$. Moreover, their period in the flow is the same, $T_{fp} \approx 0.399$. We have used standard numerical algorithms to find the location and period of these unstable fixed points [29]. These are related to unstable periodic orbits of the flow, where only a single pair of the corresponding six Floquet multipliers differs from 1. These two multipliers are $-0.703\,123$ and $-1.422\,23$. Initial conditions in a small neighborhood of these unstable periodic orbits also give rise to the TSL.

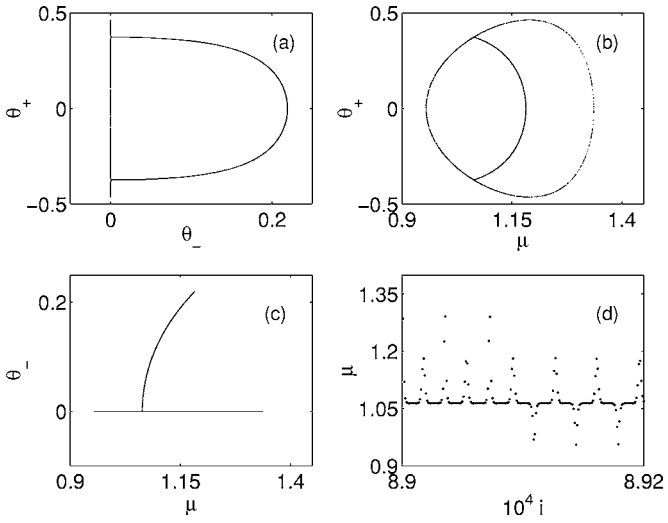

FIG. 4. Different projections for the Poincaré return map of the TSL when $\delta_3 = -16/15$. (a) Projection onto the plane (θ_-, θ_+) for a time interval containing both regions A and B. (b) Projection onto the plane (μ, θ_+). (c) Projection onto the plane (μ, θ_-). (d) Plot of μ versus the iterate i for the same TSL as in (a). Here we can see the laminar intervals.

In the return map, μ has almost regular motion within the two STRs. The time series of Fig. 4(d) alternates between almost regular intervals, also known as laminar, and disordered behavior in an irregular fashion. During these disordered intervals, μ looks like a short and large burst, which occurs whenever the orbit leaves any of the two STRs. The continuous-time trajectory of Figs. 3(a) and 3(b) is the same orbit which we show in Fig. 4(d), where μ is sampled at the Poincaré section. At a qualitative level, a better understanding of the intermittent behavior is gained by the observation that the trajectory is repeatedly reinjected back to the STRs, which, in turn, leads to laminar behavior. This suggests to us that within each STR there is a hyperbolic fixed point of the return map, whose stable and unstable manifolds are responsible for the observed chaotic behavior. Indeed, the dynamics of thin stochastic layers in a mapping is typically determined by the complex structure near the hyperbolic fixed points, where the orbits spend more time than in other parts of the phase space [5]. This is suggested by Fig. 4(d). The TSL complex structure is appreciated in Fig. 5(a), where one of the two STRs has been projected onto the (μ, θ_-) plane. Here there is a divided phase space where regular and chaotic regions coexist. The presence of islands in this figure sug-

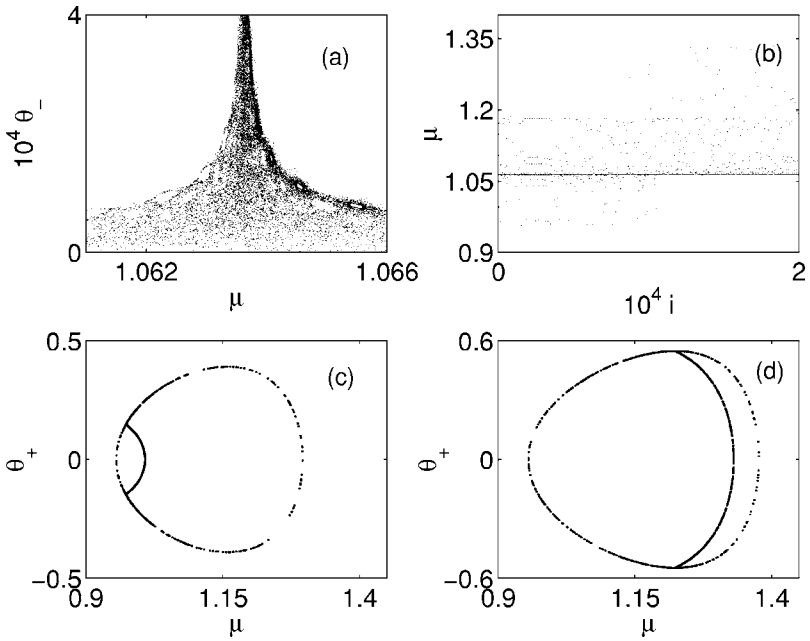

FIG. 5. (a) Magnification of the symmetric trapping region (STR) projected onto the (μ, θ_-) plane. (b) Plot of μ versus the iterate i. Here, we can see sticky parts of the trajectory having almost regular oscillations in the trapping domains. $\delta_3 = -16/15$ in (a) and (b). (c) Projection of the TSL onto the plane (μ, θ_+) when $\delta_3 = -0.9$. (d) Same as (c) but when $\delta_3 = -1.25$.

gests the relevance of self-similar structures, where a trajectory can be trapped temporarily. These traps influence to a great extent the transport properties of Hamiltonian systems [30] and can be attributed to the sticky domains that belong to boundaries of KAM islands and cantori [3,30]. The structure of thin stochastic layers is determined to a good extent by the mutual positions and sizes of embedded KAM islands [5]. The presence of these trapping domains is suggested by Fig. 5(b). Typically, these traps are related to periodic orbits whose periods are much larger than 1, as shown in Fig. 5(b). Indeed, in the TSL, we found only a single pair of hyperbolic fixed points of the map, which we considered above. Moreover, we found numerical evidence that the residence time within the trapping domains typically increases as the parameter $\delta_3 < 0$ increases in absolute value.

Our TSL has, roughly speaking, three different types of intermittency, namely, a reinjection and trapping mechanism in the neighborhood of two hyperbolic fixed points. This happens within the shortest time scales, as shown in Fig. 4(d). In contrast, the time scales of transport between regions A and B, as shown in Figs. 3(c) and 3(d), are much longer, i.e., roughly 10^5 map iterations. Moreover, within the trapping domains near KAM islands, an orbit stays typically for an intermediate number of iterations. All this occurs when δ_3 lies roughly between $-13/15$ and $-19/15$ with the aforesaid set of initial conditions. This suggests that our TSL is generic. This is illustrated in Figs. 5(c) and 5(d) for which $\delta_3 = -0.9$ and -1.25, respectively, where the norm N and the initial conditions are the same as those in Fig. 4. As suggested by Figs. 4(a) and 4(b) the Poincaré map has the symmetry $(\mu, \theta_+, \theta_-) \to (\mu, -\theta_+, \theta_-)$. This symmetry of the map presumably arises as a result of the induced mirror symmetry in our system, i.e., $N_{1,2} \to N_{2,1}$, $\theta_{1,2} \to \theta_{2,1}$, $N_3 \to N_3$, $\theta_3 \to \theta_3$.

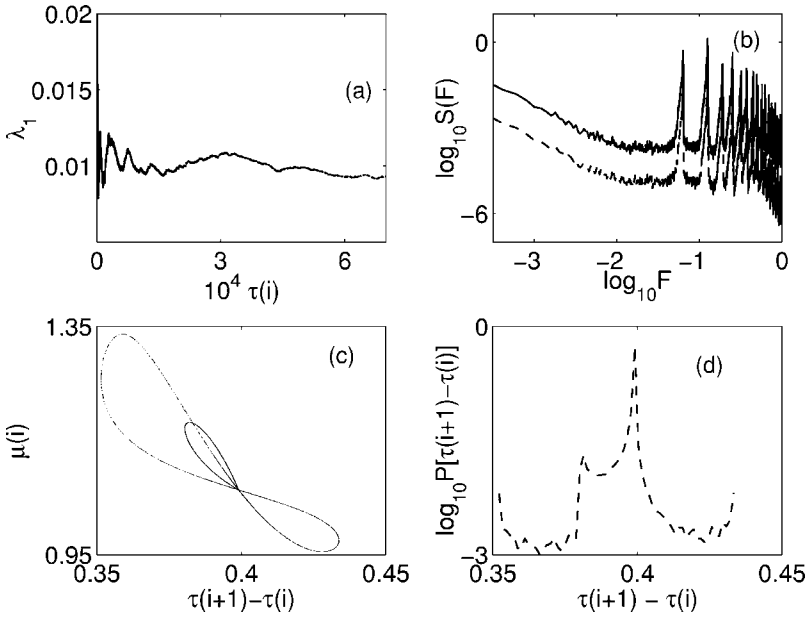

FIG. 6. (a) Plot of the Lyapunov exponent λ_1 versus time $\tau(i)$ at the Poincaré section. (b) Plot of the power spectra $\log_{10}S(F)$ versus $\log_{10}F$ for $\tau_{i+1} - \tau_i$ (dashed line) and $\mu(i)$ (solid line). (c) Plot of $\tau_{i+1} - \tau_i$ versus $\mu(i)$. (d) Histogram of the Poincaré cycles $\log_{10}P(\tau_{i+1} - \tau_i)$. In these figures the same TSL has been considered, where $\delta_3 = -16/15$.

B. The indicators of chaos

The standard indicator of chaos consists in the existence of, at least, a single positive Lyapunov exponent [1]. Our autonomous Hamiltonian system has three Lyapunov exponents, namely, $(\lambda_1, 0, -\lambda_1)$. The evolution of λ_1 with time is indicated in Fig. 6(a).

In Fig. 6(b) we can appreciate the power spectra $S(F)$ of the time series $\mu(i)$ and $\tau(i+1)-\tau(i)$. Both power spectra $S(F)$ look the same except for a constant factor, which makes the difference in Fig. 6(b). The low-frequency components of the power spectra exhibit a power-law dependence, while the dependence on the highest frequencies shows slightly broadband peaks. Both features are indicators of chaotic behavior [1].

To give a qualitative explanation to the proportionality of these power spectra $S(F)$, we first plot $\mu(i)$ versus $\tau(i+1)-\tau(i)$. This is done in Fig. 6(c), where the plot describes a seemingly smooth closed curve, the TSL, whose width is several orders of magnitude smaller than the typical scale of the full trajectory. Our qualitative argument, to explain the likeness of the power spectra $S(F)$ in Fig. 6(b), is based on a condition imposed on the equations of smooth plane closed curves, whose variables are related to some expansion in terms of periodic functions, such as the epitrochoid [31]. The parametric equations for an epitrochoid are $x(w)=(a+b)\cos(w)-c\cos[(a+b)w/b], y(w)=(a+b)\sin(w)-c\sin[(a+b)w/b]$, where a, b, and c are positive constant parameters [31]. Notice that the amplitudes and frequencies of the trigonometric components of $x(w)$ and $y(w)$ are precisely the same. We choose a given time series w_i such that the parametric equations $x(w_i)$ and $y(w_i)$ cover most of the closed curve. Next, we look for a condition that brings about similar power spectra for $x(w_i)$ and $y(w_i)$. To this end, we calculate, first, the autocorrelation function (ACF) [1] for both $x(w_i)$ and $y(w_i)$. As a result, the relation

$$\left|\left\langle (a+b)^2\cos(w_{i+L}-w_i)+c^2\cos\left(\frac{a+b}{b}w_{i+L}-\frac{a+b}{b}w_i\right)-c(a+b)\cos\left(w_{i+L}-\frac{a+b}{b}w_i\right)-c(a+b)\cos\left(\frac{a+b}{b}w_{i+L}-w_i\right)\right\rangle\right|$$
$$\gg\left|\left\langle (a+b)^2\cos(w_{i+L}+w_i)+c^2\cos\left(\frac{a+b}{b}w_{i+L}+\frac{a+b}{b}w_i\right)-c(a+b)\cos\left(w_{i+L}+\frac{a+b}{b}w_i\right)-c(a+b)\cos\left(\frac{a+b}{b}w_{i+L}+w_i\right)\right\rangle\right|$$

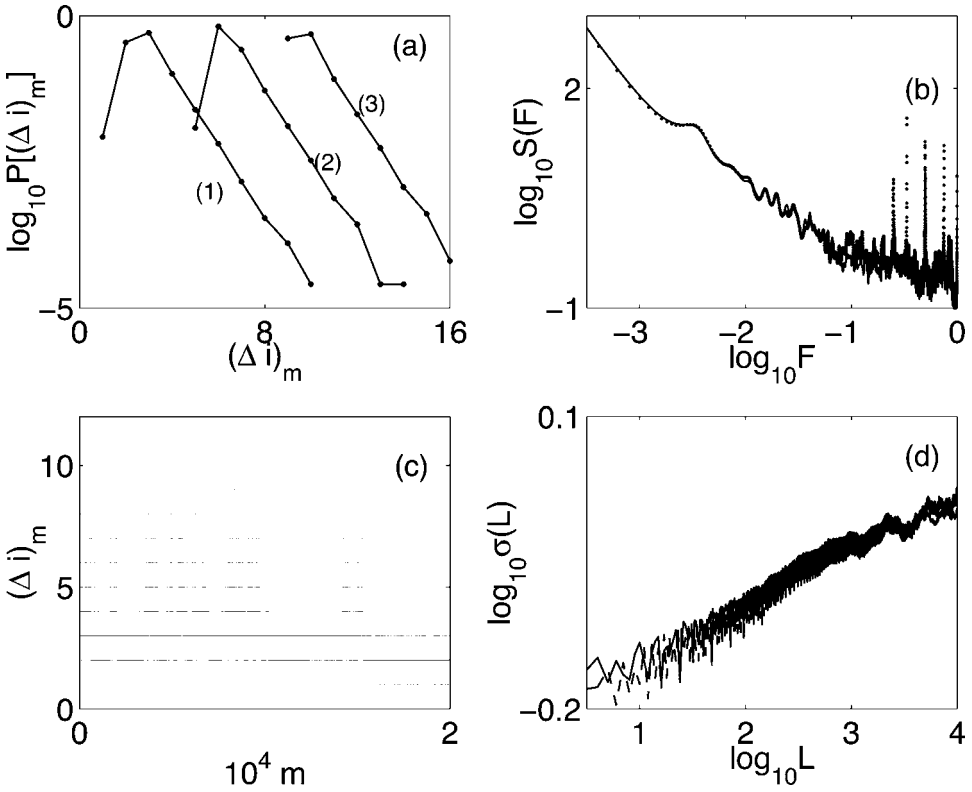

FIG. 7. (a) Histograms of the transit times $\log_{10}P[(\Delta i)_m]$ for $\rho=0.0001$ (line 1), 0.001 (line 2), and 0.01 (line 3). (b) Plot of the power spectra $\log_{10}S(F)$ versus $\log_{10}F$ for the transit times $(\Delta i)_m$ for $\rho=0.0001$ (dotted line) and 0.001 (solid line). (c) Plot of $(\Delta i)_m$ versus m when $\rho=0.0001$. (d) Plot of $\log_{10}\sigma(L)$ versus $\log_{10}L$ for $(\Delta i)_m$ when $\rho=0.0001$ (dotted line) and 0.001 (solid line). The associated slope defines the Hurst exponent h. In these figures the same TSL has been considered, where $\delta_3=-16/15$.

must hold to make the ACFs for both $x(w_i)$ and $y(w_i)$ basically proportional. We are assuming that the time series w_i is stationary. As a result, the ACF depends only on the time difference L between w_i and w_{i+L}, which is called the lag [32]. The proportionality factor depends on the ratio of $\langle x(w_i)^2\rangle$ to $\langle y(w_i)^2\rangle$. $\langle\cdots\rangle$ stands for the sample average. Moreover, as a result of the Wiener-Khintchine theorem [32], proportionality between the ACFs for $x(w_i)$ and $y(w_i)$ implies proportionality between their associated power spectra $S(F)$. That is precisely what we see in Fig. 6(b). This observation suggests to us that for $\mu(i)$ and $\tau(i+1)-\tau(i)$ there is a coarse-grained description qualitatively similar to that of parametric curves, which approximates better at scales much larger than the width of the TSL. This qualitative description, therefore, could not reproduce the TSL fine structure.

The probability distribution function (PDF) of $\tau(i+1)-\tau(i)$ is shown in Fig. 6(d). This histogram shows a clearcut global maximum at $\tau(i+1)-\tau(i)\approx 0.4$. This maximum corresponds to the aforesaid periodicity T_{fp} of the hyperbolic fixed points. This maximum reflects the frequent reinjections towards these fixed points and the length of the transit times.

VI. TRANSIT TIME DYNAMICS

A. The trimer

Consider the evolution of $\mu(i)$, shown in Fig. 4(d). We trace a small neighborhood in the $\mu(i)$ axis, which contains the laminar intervals in Fig. 4(d). The widths of these neighborhoods are $\rho=10^{-4}$, 10^{-3}, and, finally 10^{-2}. In all cases, the orbit of the return map consecutively alternates between the two STRs. Then, we look for the probability density function of the transit times for an orbit to traverse these neighborhoods, i.e., we look for the distribution of the lengths of the laminar intervals $(\Delta i)_m$, where m labels the order in this sequence. These histograms are depicted in Fig. 7(a). The bigger the width of the neighborhood, the more shifted to the right these distributions are, indicating that the trajectory can spend a longer time within a larger neighborhood. Indeed, the average transit time to traverse a suitable set is proportional to some measure of this set [33]. We point out that these PDFs decay exponentially fast for the largest laminar intervals $(\Delta i)_m$, while for smaller intervals the distributions have a maximum. It is known that the distribution of the transit times for hyperbolic systems has an exponential decay [33]. Notice that all these PDFs have to a good degree the same robust exponential decay.

The power spectra $S(F)$ of the time series $(\Delta i)_m$ display a low-frequency dependence which scales with F over more than two orders of magnitude. Indeed, $S(F)\sim F^{-1.35}$ as shown in Fig. 7(b). In this figure the time series $(\Delta i)_m$ were generated using as widths $\rho=10^{-3}$ and 10^{-4}. Based on Fig. 7(b), we may argue that, to some extent, there is self-similarity in the low-frequency components of the time series $(\Delta i)_m$. Indeed, that is what we see qualitatively in Fig. 7(c), where the value of $(\Delta i)_m$ with the largest probability, $(\Delta i)_m=3$, is highly persistent, indicating long-range correlations. In Fig. 7(c) the time series was generated using a neighborhood with $\rho=10^{-4}$. Similar results were obtained using other neighborhoods. Therefore, our model generates infrequent hopping in a system with a discrete state space given by the different laminar intervals $(\Delta i)_m$. This kind of mechanism contains the essential features of systems whose power spectra display power-law dependence. A class of one-dimensional maps with a hopping mechanism, showing $1/f$ noise, was considered some time ago [34].

To quantify the extent of self-similarity, we have calculated the Hurst exponent h, which is defined as the slope of the curve $\log_{10}\sigma(L)$ versus $\log_{10}L$, where

$$\sigma(L)=\left(\frac{1}{R-L}\sum_{m=1}^{R-L}|(\Delta i)_{m+L}-(\Delta i)_m|^2\right)^{1/2}.$$

R is the amount of data and L is the corresponding lag. We find that $h\sim 0.1$ for about two orders of magnitude of the lag L as shown in Fig. 7(d). In this figure, the time series were generated using $\rho=10^{-3}$ and 10^{-4}. For very large lag L, the time series $(\Delta i)_m$ does not grow any further. That is why we see saturation of the variance $\sigma(L)$. A value of the Hurst exponent h smaller than $\frac{1}{2}$, as in our case, indicates that we are dealing with a subdiffusive process on scales where $L<10^3$.

For the sake of completeness, we consider the transit times to traverse the region of phase space where $\theta_+<0$. This symbolic dynamics approach is based on the aforesaid symmetry $(\mu,\theta_+,\theta_-)\to(\mu,-\theta_+,\theta_-)$. Notice that now $(\Delta i)_m$ contains intervals in the laminar phase as well as bursting intervals. As a result of our numerical calculations, we found that the power spectra $S(F)$ and the Hurst exponent h for this new time series remain basically the same as those calculated above. This result suggests to us the relevant contribution of the laminar intervals.

B. The standard map

Consider a thin stochastic layer of the standard map to compare its transit time dynamics with that of the trimer. The standard map is defined on the two-dimensional torus and is given by the following [1]:

$$X_{n+1}=X_n+P_{n+1},$$

$$P_{n+1}=P_n+K\sin(X_n). \tag{8}$$

Both X_n and P_n are modulo 2π and are given in the interval $(-\pi,\pi)$. If $K>0$ the map has a hyperbolic fixed point at $(0,0)$. The largest eigenvalue of the matrix of the linear part of this map is $1+K/2+\sqrt{K+K^2/4}$. Therefore, the stable and unstable manifolds of $(0,0)$ intersect for $K>0$, creating the so-called thin stochastic layer. The width is one of the main characteristics of the TSL. It is conjectured that this width is of the order of $O(\exp(-\text{const}/\sqrt{K}))$ for $K\ll 1$ [35]. We choose the parameter $K=0.17$; therefore, most of the phase space is filled with KAM tori.

We trace a small circle of radius $\rho=10^{-2}$ centered at the hyperbolic point $(0,0)$. The time series $(\Delta i)_m$ of the transit times for an orbit to traverse this circle is shown in Fig. 8(a). The PDF of this time series is displayed in Fig. 8(b). We see

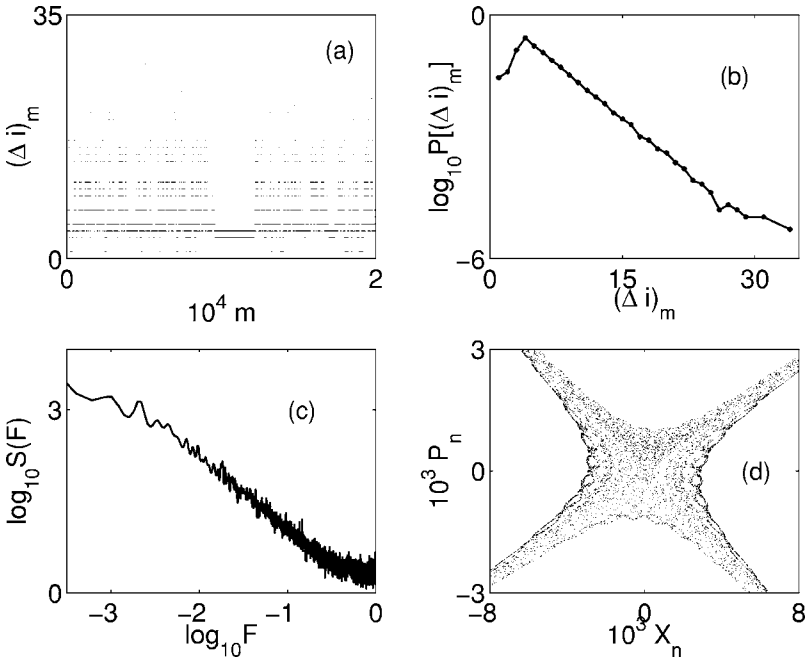

FIG. 8. (a) Plot of the laminar intervals $(\Delta i)_m$ in the standard map. Here, in the neighborhood of the hyperbolic fixed point $(0,0)$, we considered $\rho=0.01$. (b) Histogram of $(\Delta_i)_m$. (c) Plot of the power spectrum $\log_{10}S(F)$ versus $\log_{10}F$ for $(\Delta_i)_m$. (d) Magnification of a neighborhood of $(0,0)$. In these figures the same stochastic layer has been considered, where $K=0.17$.

that both are reminiscent of the TSL of the DNLSE. Indeed, Fig. 8(a) exhibits a marked persistence of $(\Delta i)_m$ in the standard map, exactly as Fig. 7(c) did for the DNLSE. The structure of the PDFs in Fig. 8(b) is consistent with those PDFs of Fig. 7(a). The power spectrum $S(F)$ in Fig. 8(c) for the standard map and those of Fig. 7(b) for the DNLSE display a power-law dependence on the frequencies F for about two orders of magnitude. Finally, a magnification of the neighborhood of the hyperbolic fixed point $(0,0)$ for the standard map shows the characteristic complex island structure which arises also at the STR in Fig. 5(a). By the same token, in the standard map we observe that the typical time scale of the laminar intervals $(\Delta i)_m$ is much smaller than that of the trapping domains. This reminds us of the time scales of Figs. 4(d) and 5(b) computed for the DNLSE. This comparison allowed us to see the usefulness of this approach to extract symbolic dynamics embedded in the TSL. We believe that this kind of symbolic dynamics deserves further consideration, at least as a way to characterize the TSL solutions. In the standard map, as in the trimer case, the long-range correlations result from an infrequent hopping mechanism in a system with a discrete state space, which is given by the different integer values of $(\Delta i)_m$.

VII. LOCAL INTERFERENCE IN A RING OF WEAKLY COUPLED BECs

In this section we will consider a possible experimental situation, where the observation of physical quantities in the laminar and bursting intervals can be carried out. Equation (1) has been derived from the Gross-Pitaevskii equation when the height of the optical potential is strong enough. In this case, the tight-binding approximation holds and the lowest band dynamics maps onto the DNLSE [11]. Under these conditions, the single-band Bose-Hubbard model describes this quantum system, which becomes the DNLSE when the number of trapped atoms is not small enough in the multiwell lattice [36]. In this context, the TSL is characterized by intermittency in the inversion of populations, as well as in the relative phase, between the two spatially symmetric BECs.

One of the manifestations of the wave nature of Bose-Einstein condensates is the observation of interference when the condensed and initially separated clouds of atoms are allowed to overlap [37]. This is carried out in experiments by turning off, after different evolution times, both the magnetic and optical traps. Therefore, upon expansion the condensates overlap and interfere, and if the effects of particle interactions in the overlap region can be neglected, the particle density at any point on the central axis of the ring of atoms, which is perpendicular to the plane of the ring, is proportional to

$$Q(\tau) = \left| \sum_{m=1}^{M} \psi_m \right|^2 . \tag{9}$$

If $Q(\tau)$ is measured just after the traps are turned off at τ, we can have an idea of the dynamics by considering several evolution times τ of the same system in different realizations. The particle density will depend dramatically on the relative phase of the two symmetric BECs. This is suggested by Figs. 9(a) and 9(c), which show the good degree of simultaneity between the bursting intervals of $\theta_1-\theta_2$ and those time intervals where the envelope of $Q(\tau)$ slowly drops and rises. Moreover, the bursting time intervals of ν and $\theta_1-\theta_2$ are correlated, as suggested by Figs. 3(a) and 3(b). Outside these bursting intervals, $Q(\tau)$ has relatively regular and fast oscillations, as shown in Fig. 9(b).

To assess the possibility of an experiment, consider Eq. (1) for which the particle's conservation law takes the form $N_{tot}=\Sigma_{m=1}^{M}|\Psi_m|^2$. Here N_{tot} stands for the total number of atoms in the experiment. Moreover, since $|\psi_m|$

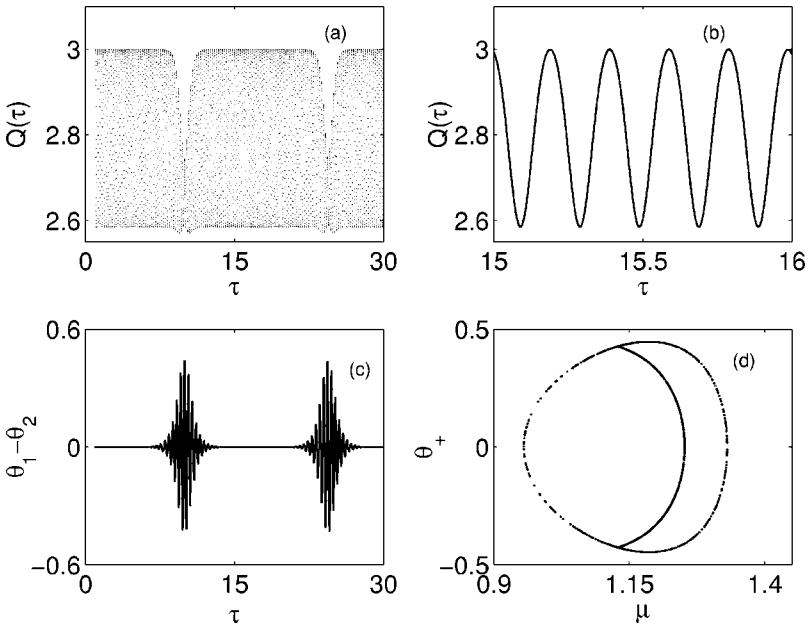

FIG. 9. (a) Continuous-time evolution of the particle density $Q(\tau)$ versus τ, for the TSL when $\delta_3=-16/15$. The slow changes of the $Q(\tau)$ envelope coincide with the bursting intervals, as suggested by (a) and (c). (b) Magnification of a laminar time interval in (a). (c) Continuous-time plot of $\theta_1-\theta_2$ versus τ. τ has been rescaled by dividing by 3π. (d) Projection of the TSL onto the plane (μ,θ_+) when $\delta_3=-1$ and $N=1.1$.

$=\sqrt{\rho/2K}|\Psi_m|$, we get the expression $\zeta(\Sigma_{m=1}^{M}|\psi_m|^2)=\frac{1}{2}$, where $\zeta\equiv K/\rho N_{tot}$. Using initial conditions in a small neighborhood of the uniform solution, where $N=1$, we find that $\Sigma_{m=1}^{3}|\psi_m|^2\approx 1$ and therefore $\zeta\approx\frac{1}{2}$. It has been suggested that the range $0<\zeta<4$ is suitable for a physical experiment consisting of a ring with three condensates [38].

Our estimates, $K\approx 0.07E_R$ and, roughly, 1000 atoms in each well, are taken from Ref. [39], where E_R stands for the recoil energy. Using these data, we get $\rho\approx 5\times 10^{-5}E_R$ and $\Delta_3=\delta_3 K\sim 1.0E_R$ for $\delta_3=-16/15$. This defect value for Δ_3 has the order of magnitude of the interwell barrier energy in the experiments with one-dimensional Josephson junction arrays carried out with atomic Bose-Einstein condensates [39]. The slow envelope changes of $Q(\tau)$, shown in Fig. 9(a), take place within 5 units of the rescaled time τ. This corresponds to a time interval of roughly 0.5 s. In contrast, the fast oscillations of $Q(\tau)$, which take place during the laminar intervals, are to a good extent repeated every 0.2 units of τ. This is shown in Fig. 9(b). This corresponds approximately to a time interval of 0.02 s. In these numerical calculations, we used the relation $3\pi\tau=Kt$, which arises from Eq. (2) and the rescaling of τ as shown in Figs. 3(a) and 3(b).

In Fig. 9(d), we can appreciate qualitatively the same TSL discussed before. This time, however, the norm is different, $N=1.1$, $\delta_3=-1.0$, and the initial conditions are within small neighborhoods of the stable stationary uniform solution, where $\psi_1=\psi_2=\psi_3$. The different ranges of N and δ_3 where the TSL arises, as shown by Figs. 4(c), 4(d), and 9(d), suggest that these stochastic layers are generic. The experimental feasibility of making few-site BEC lattices is within the reach of current technology [40]. Indeed, a recent proposal to study rings of BECs, using the tranverse electromagnetic modes of laser beams, has been reported [41]. Moreover, the relative phase of two spatially separated BECs has been continuously sampled in a recent experiment [40,42]. All this suggests that the experimental study of the behavior of $\theta_1-\theta_2$ and $Q(\tau)$ might indicate the presence of TSL dynamics in a trimer of BECs.

VIII. CONCLUSIONS AND DISCUSSION

In our model we make use of numerical continuation to investigate the dependence of different families of stationary and periodic solutions on a defect parameter, which induces mirror symmetry. The dependence on the period of the solution has also been studied. In particular we have considered a branch point where, due to the symmetry of the model, several families of stationary solutions arise. Recently, this issue has been discussed by Buonsante *et al.* [43].

Initial conditions in a small neighborhood of suitable uniform solutions give rise to generic thin stochastic layers (TSLs). We constructed a Poincaré section, where a two-dimensional manifold contains the Poincaré return map. Our TSL has, broadly speaking, three different types of intermittency. First, there is a reinjection and trapping mechanism in the neighborhood of two hyperbolic fixed points. This happens within the shortest time scales, as shown in Fig. 4(d). Second, the time scales of transport between two almost invariant regions A and B, as shown in Figs. 3(c) and 3(d), are typically much longer, i.e., roughly 10^5 map iterations. Third, within the trapping domains near KAM islands an orbit stays typically an intermediate number of iterations, as shown in Fig. 5(b). The unstable periodic orbits of the flow associated with the above mentioned hyperbolic fixed points of the return map have been found. These fixed points are embedded within the TSL. As for the standard indicators of chaos, we have explained qualitatively the proportionality between the power spectra of Poincaré cycles and a suitable action variable. These power spectra have broadband peaks and a power-law dependence on the low frequencies. These are features of chaotic behavior along with the calculated positive Lyapunov exponent.

The persistent time series of transit times, to cross some suitable sets in the Poincaré return map, generate $1/f$ noise over a wide range of parameters of the DNLSE. This is a robust property of the system, which is the result of an infrequent hopping mechanism in a discrete state space of transit times. These long-range correlations are found in different

neighborhoods for the transit times, suggesting the relevant contribution of the laminar intervals. The shape of the probability density distribution for the transit times has a maximum and a tail with an almost invariant exponential decay. The aforementioned long-memory effects are nicely portrayed in the behavior of suitable transit times in the standard map.

Finally, we have considered a possible experimental situation to follow the evolution of particle densities. We believe that two salient features of particle densities are relevant to this end, namely, the slow envelope changes, on the one hand, and the almost regular and fast oscillations, on the other hand. The former is correlated with the bursting intervals while the latter is inherent to the laminar intervals of the relative phase between the two symmetric BEC in the trimer.

We believe that further work needs to be carried out to explore the wealth of interesting behavior hidden in the study of small-size nonlinear lattices, such as DNLS lattices, where defects are a relevant ingredient in the dynamics.

ACKNOWLEDGMENTS

This work was supported by CONACYT-México and the International Centre for Theoretical Physics (ICTP). The work of E.J.D. was supported by a Discovery Grant from NSERC Canada.

[1] A. J. Lichtenberg and M. A. Lieberman, *Regular And Stochastic Motion* (Springer-Verlag, Berlin, 1993).
[2] C. F. F. Karney, Physica D **8**, 360 (1983); B. V. Chirikov and D. L. Shepeliansky, *ibid.* **13**, 395 (1984).
[3] J. D. Meiss, Rev. Mod. Phys. **64**, 795 (1992).
[4] T. Geisel, A. Zacherl, and G. Radons, Phys. Rev. Lett. **59**, 2503 (1987); **61**, 1040 (1988).
[5] S. S. Abdullaev, Phys. Rev. E **62**, 3508 (2000).
[6] P. G. Kevrekidis, K. O. Rasmussen, and A. R. Bishop, Int. J. Mod. Phys. B **15**, 2833 (2001); M. Johansson and S. Aubry, Nonlinearity **10**, 1151 (1997); D. Hennig and G. P. Tsironis, Phys. Rep. **307**, 334 (1999); D. K. Campbell, S. Flach, and Y. S. Kivshar, Phys. Today **57**(1), 43 (2004).
[7] Y. S. Kivshar and M. Peyrard, Phys. Rev. A **46**, 3198 (1992).
[8] D. N. Christodoulides and R. I. Joseph, Opt. Lett. **13**, 794 (1988).
[9] D. N. Christodoulides, F. Lederer, and Y. Silberberg, Nature (London) **424**, 817 (2003).
[10] A. Scott, *Nonlinear Science: Emergence And Dynamics Of Coherent Stuctures*, 2nd ed. (Oxford University Press, New York, 2003).
[11] A. Trombettoni and A. Smerzi, Phys. Rev. Lett. **86**, 2353 (2001); A. Trombettoni, A. Smerzi, and A. R. Bishop, Phys. Rev. E **67**, 016607 (2003).
[12] J. C. Eilbeck, P. S. Lomdahl, and A. C. Scott, Physica D **16**, 318 (1985).
[13] J. H. Jensen *et al.*, Phys. Lett. **110A**, 429 (1985); S. De Filippo, M. Fusco Girard, and M. Salerno, Physica D **26**, 411 (1987); K. W. DeLong, J. Yumoto, and N. Finlayson, *ibid.* **54**, 36 (1991); L. Cruzeiro-Hansson *et al.*, Phys. Rev. B **42**, 522 (1990); D. Hennig *et al.*, Phys. Rev. E **51**, 2870 (1995); M. Johansson, J. Phys. A **37**, 2201 (2004); R. Franzosi and V. Penna, Phys. Rev. E **67**, 046227 (2003).
[14] D. Hennig and H. Gabriel, J. Phys. A **28**, 3749 (1995).
[15] C. L. Pando L. and E. J. Doedel, Phys. Rev. E **69**, 036603 (2004).
[16] C. L. Pando L. and E. J. Doedel, Phys. Rev. E **71**, 056201 (2005).
[17] C. L. Pando L., e-print nlin-sys/0305011.
[18] H. E. Stanley *et al.*, Physica A **224**, 302 (1996).
[19] E. Faleiro *et al.*, Phys. Rev. Lett. **93**, 244101 (2004).
[20] F. Dalfovo, S. Giorgini, L. P. Pitaevskii, and S. Stringari, Rev. Mod. Phys. **71**, 463 (1999).
[21] D. Hennig and H. Gabriel, Phys. Rev. E **57**, 2371 (1998); D. Hennig, K. O. Rasmussen, H. Gabriel, and A. Bülow, *ibid.* **54**, 5788 (1996).
[22] T. Bountis, H. W. Capel, M. Kollmann, J. C. Ross, J. M. Bergamin, and J. P. van der Weele, Phys. Lett. A **268**, 50 (2000).
[23] C. L. Pando L., Phys. Lett. A **309**, 68 (2003).
[24] E. J. Doedel, H. B. Keller, and J. P. Kernévez, Int. J. Bifurcation Chaos Appl. Sci. Eng. **1**, 493 (1991).
[25] E. J. Doedel, H. B. Keller, and J. P. Kernévez, Int. J. Bifurcation Chaos Appl. Sci. Eng. **1**, 745 (1991).
[26] A. M. Lyapunov, Ann. Fac. Sci. Univ. Toulouse Sci. Math. Sci. Phys. **2**, 203 (1907).
[27] M. Dellnitz *et al.*, Int. J. Bifurcation Chaos Appl. Sci. Eng. **15**, 699 (2005).
[28] S. Wiggins, *Chaotic Transport in Dynamical Systems* (Springer-Verlag, New York, 1992).
[29] H. Kantz and T. Schreiber, *Nonlinear Time Series Analysis* (Cambridge University Press, Cambridge, U.K., 1997).
[30] G. M. Zaslavsky, Phys. Rep. **371**, 461 (2002).
[31] J. D. Lawrence, *A Catalog of Special Plane Curves* (Dover, New York, 1972).
[32] C. Chatfield, *The Analysis of Time Series: An Introduction*, 6th ed. (CRC Press, London, 2004).
[33] J. D. Meiss, Chaos **7**, 139 (1997).
[34] A. Ben-Mizrachi *et al.*, Phys. Rev. A **31**, 1830 (1985).
[35] V. G. Gelfreich, V. F. Lazutkin, and N. V. Svanidze, Physica D **71**, 82 (1994).
[36] P. Buonsante, V. Penna, and A. Vezzani, Phys. Rev. A **72**, 043620 (2005); M.W. Jack and M. Yamashita, *ibid.* **71**, 023610 (2005).
[37] M. R. Andrews *et al.*, Science **275**, 637 (1997).
[38] P. Buonsante, R. Franzosi, and V. Penna, Phys. Rev. Lett. **90**, 050404 (2003).
[39] F. S. Cataliotti *et al.*, Science **293**, 843 (2001).
[40] M. Saba *et al.*, Science **307**, 1945 (2005).
[41] L. Amico, A. Osterloh, and F. Cataliotti, Phys. Rev. Lett. **95**, 063201 (2005).
[42] Y. Shin *et al.*, Phys. Rev. Lett. **92**, 050405 (2004).
[43] P. Buonsante *et al.*, e-print cond-mat/0604372.